文章编号:1001 - 9014(2013)06 - 0491 - 08

DOI:10.3724/SP. J. 1010. 2013. 00491

A nonuniformity correction method based on Bayesian framework

QIAN Wei-Xian[1,2*], REN Jian-Le[1,2], CHEN Qian[1,2], GU Guo-Hua[1,2]

(1. Jiangsu Key Laboratory of Spectral Imaging & Intelligent Sense, Nanjing Univereity of Science and Technology, Nanjing 210094, China;
2. Key Laboratory of Photoelectronic Imaging Technology and System, Ministry of Education of China,
Nanjing University of Science and Technology, Nanjing 210094, China)

Abstract: In this study, we have created a bridge, which can connect the reference-based NUC and scene-based NUC. The right probability of the scene-based NUC parameters was calculated based on the Bayesian framework. The right probability composed of prior and observation probability was used to determine whether the calculated scene-based NUC parameters are suitable to correct the nonuniformity. The local same distribution constraint is defined in this paper, and the Infrared Focal Plane (IRFPA) gain space relativity has been discovered from the reference-based parameters by this paper firstly. The Bayesian prior probability is mainly determined by the local same distribution constraint, and the Bayesian observation probability is mainly determined by the IRFPA gain space relativity. This method can effectively balance the relationship between convergence speed and ghosting artifacts. Finally, the real and simulated infrared image sequences have been applied to demonstrate our algorithm's positive effect.

Key words: scene-based nonuniformity correction, convergence, ghosting artifacts, Bayesian

PACS: 07. 57. Kp

采用贝叶斯框架的非均匀性校正方法

钱惟贤[1,2*], 任建乐[1,2], 陈 钱[1,2], 顾国华[1,2]

(1. 南京理工大学 江苏省光谱成像与多维感知点实验室,江苏 南京 210094;
2. 南京理工大学 光电成像技术与系统教育部重点实验室,江苏 南京 210094)

摘要:提出了一种在基于场景非均匀性校正和定标非均匀性校正之间建立桥梁的思路,利用定标法提供的大量先验信息解决收敛速度和鬼影的矛盾问题. 利用贝叶斯方法计算非均匀性参数的正确概率,用参数正确概率来决定是否使用该组参数进行校正,从而在源头上抑制鬼影. 对于先验概率,定义了非均匀性的局部同分布约束,并通过定标统计的策略利用该约束构建了先验概率;对于观测概率,发现并详细分析了红外焦平面阵列固有的非均匀增益参数空间相关性,利用空间相关性构建了观测概率. 最终,通过本文算法对真实和仿真的红外图像序列进行处理,表明该算法在保证高收敛速度前提下,其参数正确概率有效抑制了鬼影,取得了好的处理效果.

关 键 词:基于场景非均匀性校正;收敛;鬼影;贝叶斯

中图分类号:TN215 **文献标识码**:A

Introduction

At present, convergence and ghosting artifacts are common problems in the scene-based nonuniformity correction (NUC) algorithms. A number of researchers have developed scene-based algorithms for NUC. D. A. Scribner et al. introduced the LMS-based NUC algorithm[1] and the temporal high-pass NUC algo-

Received date: 2012 - 07 - 29, **revised date**: 2013 - 04 - 16 **收稿日期**:2012 - 07 - 29, **修回日期**:2013 - 04 - 16

Foundation items: Supported by the National Natural Science Foundation of China (61101199), Jiangsu Province Natural Science Foundation of China (BK2011699), Program for New Century Excellent Talents in University (NCET - 12 - 0630), Key Project of Independence Research of Nanjing University of Sci & Tech (20112DJH22)

Biography: 钱惟贤(1980-),男,江苏金湖人,南京理工大学电光学院,博士,主要从事红外成像电子学与目标探测研究. E-mail: developer_plus@163. com.

* **Corresponding author**: E-mail: developer_plus@163. com

rithm[2]. John G. Harris et al. introduced the Constant-Statistics Constraint (CS) NUC algorithm[3]. Zhang et al. presented the local CS algorithm[4]. Sergio N. Torres et al. presented the NUC algorithm based on Kalama filter[5]. Marlene Shehadeh and Oleg Kuybeda introduced the robust global motion estimation technique for NUC[6]. Qian et al. introduced the space low-pass and temporal high-pass NUC algorithm[7-8]. In fact, convergence speed and ghosting artifacts still remain as bottleneck problems in the above scene-based NUC algorithms.

Though a lot of works have been done, two core problems, convergence speed and ghosting artifacts of the scene-based NUC haven't been solved. The scene-based NUC calculates the nonuniformity parameters through the interframe iterative mode. From the mathematical point of view, the higher convergence speed means the less frames to calculate the same precision nonuniformity parameters. The higher convergence means that the algorithm is more practical. The ghosting artifacts are the wrong nonuniformity parameters calculated by the scene-based NUC. From the statistical point of view, the convergence speed and ghosting artifacts are the speed and precision of the nonuniformity parameters estimation.

Till now, when doing the scene-based NUC, the reference-based nonuniformity parameters haven't been carefully paid attention. When the traditional scene-based NUC algorithms meet the bottleneck, we have to pay attention to the ignored reference-based parameters. The main idea of this paper is to introduce a method, which can connect the scene-based parameters and the reference-based parameters.

The main spirit of the method is the Bayesian framework. The right probability of the scene-based NUC parameters is introduced in this paper. The right probability indicates whether the calculated scene-based NUC parameters are accurate. The right probability is calculated from the Bayesian framework,

This paper is organized as follows. In Section 2, the local same distribution constraint is introduced. In Section 3, the characteristic of IRFPA gain's space relativity is described in detail. In Section 4, the calculation of the NUC parameter right probability using the Bayesian framework is presented. In Section 6 and 7, to test our algorithm's processing effect include convergence speed the whole algorithm and experiments are introduced, respectively.

1 From the constant-statistics constraint to the local same distribution constraint

To make the CS algorithm[3] more usable, the same distribution constraint should be relaxed. We change it to nearly same distribution in local region and call it local same distribution. $m_{i,j}^{\text{in}}, s_{i,j}^{\text{in}}$ are the temporal mean and temporal standard deviation of the (i, j) input data. The local region size is $(2o+1)\times(2o+1)$. The new constraint implies that the input distribution into every pixel can only exists low-frequency difference. Moreover, the low-frequency difference can be eliminated.

$$\text{offset}_{i,j}(k) = m_{i,j}(k) - \frac{1}{(2o+1)^2}\sum_{p=i-o}^{i+o}\sum_{j-o}^{j+o} m_{p,q}(k) \quad , (1)$$

$$\text{gain}_{i,j}(k) = s_{i,j}(k)/\left[\frac{1}{(2o+1)^2}\sum_{p=i-o}^{i+o}\sum_{q=j-o}^{j+o} s_{p,q}(k)\right] \quad , (2)$$

$m_{i,j}(k)$ and $S_{i,j}(k)$ are the output of CS algorithm, Eqs. (1), and (2) can eliminate the low-frequency difference of input distribution. If the space standard deviation of $m_{i,j}^{\text{in}}$ and $s_{i,j}^{\text{in}}$ in the $(2o+1)\times(2o+1)$ local region are very small, it can be regarded as local same distribution.

Define

$$Y_{i,j}(k) = \begin{bmatrix} Y_{i,j}(k) \\ 1 \end{bmatrix} \quad , (3)$$

$$\theta_{i,j}(k) = \begin{bmatrix} 1/\text{gain}_{i,j}(k) \\ -\text{offset}_{i,j}(k)/\text{gain}_{i,j}(k) \end{bmatrix} \quad . (4)$$

The NUC output is

$$x_{i,j}(k) = \theta_{i,j}(k)^T \cdot Y_{i,j}(k) \quad , (5)$$

$x_{i,j}(k)$ is the NUC processed data. Define

$$Y_{i,j}^k = \{Y_{i,j}(1), Y_{i,j}(2), \cdots, Y_{i,j}(k)\} \quad , (6)$$

$$\theta_{i,j}^k = \{\theta_{i,j}(1), \theta_{i,j}(2), \cdots, \theta_{i,j}(k)\} \quad , (7)$$

$$x_{i,j}^k = \{x_{i,j}(1), x_{i,j}(2), \cdots, x_{i,j}(k)\} \quad , (8)$$

$Y_{i,j}^k$ is the known observed data, $\theta_{i,j}^k$ and are the NUC parameters which are calculated from $Y_{i,j}^k$. It can be said that if the input data obey the local same distribution constraint, the right probability of $\theta_{i,j}^k$ will increase, otherwise, the right probability of $\theta_{i,j}^k$ will decrease.

2 The IRFPA gain space relativity

In fact, human can easily judge the correctness of the nonunifority parameters when they see the images only containing the nonuniformity. From the point of view of artificial intelligence, there must exist some algorithms which can be used to judge the correctness of the nonuniformity parameters. For simple, we use the Gaussian distribution assumption of the characteristic quantities to classify the correctness of the nonuniformity parameters.

We use the IRFPA (Sofradir MARS long-wavelength 320×256 HgCdTe) to capture black-body images at different temperatures ($-40 \sim 100$℃). These images are regarded as the nonuniformity images without scene. The gain at temperature can be derived by the Eq. (9).

$$\mathrm{GAIN}_{i,j}(T) = [y_{i,j}(T+\Delta T) - y_{i,j}(T-\Delta T)] / \left\{ \frac{1}{(2o+1)^2} \sum_{p=i-o}^{i+o} \sum_{q=j-o}^{j+o} [y_{p,q}(T+\Delta T) - y_{p,q}(T-\Delta T)] \right\} . \quad (9)$$

To distinguish with scene-based $\mathrm{gain}_{i,j}(k)$, we use $\mathrm{GAIN}_{i,j}(T)$ to represent the reference-based gain at temperature T. ΔT is the temperature increment. Equation (9) can be regard as the derivative of the response curve at temperature T. In Eq. (9), gain at (i,j) is divided by its local region mean. This process can make the reference-based gain parameter distribute around 1, and make $\mathrm{GAIN}_{i,j}$ consistent with $\mathrm{gain}_{i,j}$.

The IRFPA response curve in T's neighbor temperature can be regard as linear. If ΔT is not too large, its changing has little impact on $\mathrm{gain}_{i,j}(T)$. ΔT(1℃) and ΔT(2 ℃) will obtain same $\mathrm{gain}_{i,j}(T)$. So ΔT is set 1℃ and T is set {−39℃, −38℃, −37℃ …, 98℃, 99℃}. Figure 1 is $\mathrm{GAIN}_{i,j}$ at different temperature T. o is set to 5.

We can find that the gain changes very little in the local region. So we begin to care about the space standard deviation of the gain at the local region. Equation (10) is the local region standard deviation of the gain.

$$d_{i,j}(T) = \mathrm{std}\Pi_O[\mathrm{GAIN}_{i,j}(T)] = \sqrt{\frac{\sum_{p=i-o}^{i+o} \sum_{q=j-o}^{j+o} \left\{ \mathrm{GAIN}_{p,q}(T) - \left[\sum_{g=i-o}^{i+o} \sum_{f=j-o}^{j+o} \mathrm{GAIN}_{g,f}(T)/(2o+1)^2 \right] \right\}^2}{(2o+1)^2}} , \quad (10)$$

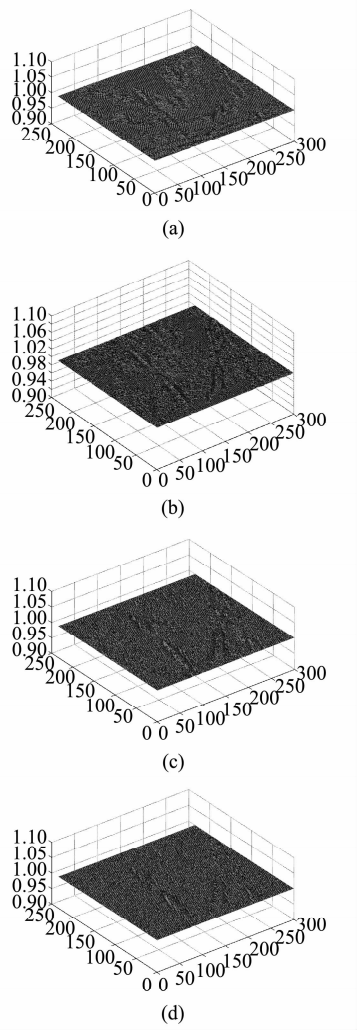

Fig. 1　$\mathrm{GAIN}_{i,j}$ at different temperature (a) −39℃, (b) 10℃, (b) 60℃, (b) 99℃
图 1　不同温度下的 $\mathrm{GAIN}_{i,j}$ (a) −39℃, (b) 10℃, (b) 60℃, (b) 99℃

$\mathrm{std}\Pi_O(\bullet)$ is the operator to calculate local region standard deviation at (i,j). $d_{i,j}(T)$ is the (i,j) local region standard deviation of the gain at temperature T. The local region size is $(2o+1)\times(2o+1)$. o is set to 5. Figure 2 is $d_{i,j}(T)'$s 3D image.

Then we calculated temperature mean and temperature standard deviation of $d_{i,j}$.

$$m_{i,j} = \frac{\sum_{T=-39}^{99} d_{i,j}(T)}{139} , \quad (11)$$

$$sd_{i,j} = \sqrt{\frac{\sum_{T=-39}^{99} [d_{i,j}(T) - m_{i,j}]^2}{139}} , \quad (12)$$

$m_{i,j}$ and $sd_{i,j}$ are the temperature mean and temperature standard deviation of $d_{i,j}$, respectively. Figure 3 (a)

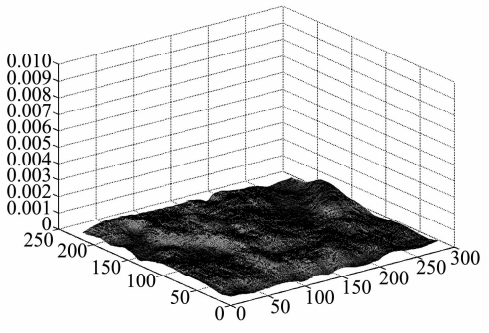

Fig. 2 $d_{i,j}(T)$'s 3D image ($T = 10$℃)
图 2 $d_{i,j}(T)$的三维图像($T = 10$℃)

and (b) are the 3D images of temperature mean and temperature standard deviation of $d_{i,j}$, respectively.

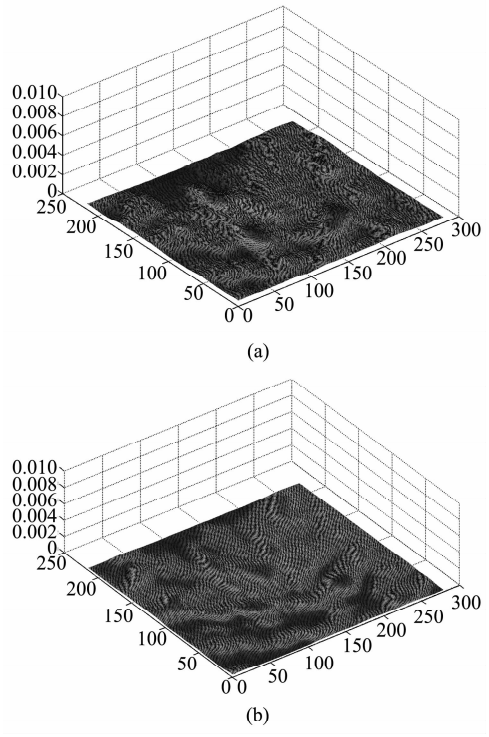

Fig. 3 3D image of $d_{i,j}$ (a) temperature mean, and (b) temperature standard deviation
图 3 $d_{i,j}$的三维图像 (a)温度域均值,(b)温度域标准差

From Fig. 3, it can be seen that the value of the local region standard deviation of the gain are very small. It represents that the gain is very close in the local region. We call it the space relativity of IRFPA gain. Then a Gaussian distribution was used to represent the probability distribution of $d_{i,j}$.

$$p(d_{i,j}) = \frac{1}{\sqrt{2\pi}\, sd_{i,j}} \exp\left[-\frac{(d_{i,j} - m_{i,j})^2}{sd_{i,j}^{\ 2}} \right] \quad (13)$$

$p(d_{i,j})$ is the probability distribution of $d_{i,j}$ at pixel (i, j). It can be said that the nonuniformity parameter of MARS long-wavelength 320 × 256 HgCdTe IRPFA should obey the distribution of Eq. (20).

$$p(\theta_{i,j}) = \frac{1}{\sqrt{2\pi}\, sd_{i,j}} \exp\left[-\frac{(d_{i,j} - m_{i,j})^2}{sd_{i,j}^{\ 2}} \right] . \quad (14)$$

If the value of $p(\theta_{i,j})$ is very small, it usually means that the calculated nonuniformity parameter will not be right.

3 The right probability of the NUC parameters

Using Eqs. (1)-(4), the NUC parameters $\theta_{i,j}(k)$ can be got. But there will be a question whether $\theta_{i,j}(k)$ is reliable or not. If it is reliable, it can be used to correct the nonuniformity and will not generate the ghosting artifacts. Otherwise, it will generate the ghosting artifacts. Here, $\kappa_{i,j}(k)$ is created to represent that $\theta_{i,j}(k)$ is correct. $p[\kappa_{i,j}(k)]$ is the right probability of $\theta_{i,j}(k)$. Because $Y_{i,j}^k$ and $\theta_{i,j}(k)$ can be regarded as the known data, $p[\kappa_{i,j}(k)]$ can be represented by a conditional probability $p[\kappa_{i,j}(k) \mid \theta_{i,j}(k), Y_{i,j}^k]$.

According to the Bayesian theory[9]

$$p[\kappa_{i,j}(k) \mid \theta_{i,j}(k), Y_{i,j}^k] = \frac{p[\kappa_{i,j}(k) \mid Y_{i,j}^k] p[\theta_{i,j}(k) \mid \kappa_{i,j}(k), Y_{i,j}^k]}{\sum p[\kappa_{i,j}(k) \mid Y_{i,j}^k] p[\theta_{i,j}(k) \mid \kappa_{i,j}(k), Y_{i,j}^k]} \propto p[\kappa_{i,j}(k) \mid Y_{i,j}^k] p[\theta_{i,j}(k) \mid \kappa_{i,j}(k), Y_{i,j}^k] \quad (15)$$

here, $p[\kappa_{i,j}(k) \mid Y_{i,j}^k]$ is the prior probability and $p[\theta_{i,j}(k) \mid \kappa_{i,j}(k), Y_{i,j}^k]$ is the observation probability. $p[\kappa_{i,j}(k) \mid Y_{i,j}^k]$ means when we only know $Y_{i,j}^k$, what is the right probability of $\theta_{i,j}(k)$ according to our experience. $p[\theta_{i,j}(k) \mid \kappa_{i,j}(k), Y_{i,j}^k]$ means when $Y_{i,j}^k$ is known and $\theta_{i,j}(k)$ is regarded as right, what is the probability that $\theta_{i,j}(k)$ take current value.

We first design the prior probability. $p[\kappa_{i,j}(k-1) \mid \theta_{i,j}(k-1), Y_{i,j}^{k-1}]$ is the posterior probability in frame $k-1$. The experience of the right probability in frame k should first come from the posterior right probability in frame $k-1$.

The prior probability should be related with the local same distribution constraint. Direct calculaton of $m_{i,j}^{\text{in}}$ and $s_{i,j}^{\text{in}}$ is difficult. So we use the space standard

deviation of $y_{i,j}(k)$ to approximately represent the local same distribution constraint. If (i,j) lies in the strong edge region, it is usually hard to satisfy the local same distribution constraint. The space local standard deviation of (i,j) can be used to represent the intensity of the edge region[11-14].

$$p_{lsd}[Y_{i,j}(k)] = \exp\left(-\frac{\mathrm{std}\Pi_O[Y_{i,j}(k)]}{\sigma_{lsd}(i,j)}\right), \quad (16)$$

$p_{lsd}[Y_{i,j}(k)]$ is the local same distribution probability. If (i,j) lies in the strong edge region, the value of $p_{lsd}[Y_{i,j}(k)]$ will be small. $\mathrm{std}\Pi_O(\bullet)$ is the operator to calculate (i,j) space local standard deviation.

$$\mathrm{std}\Pi_O[Y_{i,j}(k)] = \sqrt{\frac{\sum_{p=i-o}^{i+o}\sum_{q=j-o}^{j+o}\left\{y_{p,q}(k) - \left[\sum_{g=i-o}^{i+o}\sum_{f=j-o}^{j+o} y_{g,f}(k)/(2o+1)^2\right]\right\}^2}{(2o+1)^2}}. \quad (17)$$

Same as above, the local region size is $(2o+1)\times(2o+1)$. $\sigma_{lsd}(i,j)$ is the local standard deviation of a image, while this image must obey the local same distribution constraint. A clean sky image is a good choice. Select one clean sky image, and calculate its local standard deviation $\sigma_{lsd}(i,j)$ by Eq. (17).

According to above description, the probability $p[\kappa_{i,j}(k-1)\,|\,\theta_{i,j}(k-1), Y_{i,j}^{k-1}]$ in frame $k-1$ first comes from $p[\kappa_{i,j}(k-2)\,|\,\theta_{i,j}(k-2), Y_{i,j}^{k-2}]$. If $p_{lsd}[Y_{i,j}(k)]$ is one element of $p[\kappa_{i,j}(k)\,|\,Y_{i,j}^{k}]$, it will mean

$$p[\kappa_{i,j}(k)\,|\,Y_{i,j}^{k}] \propto p_{lsd}[Y_{i,j}(k)]\,p_{lsd}[Y_{i,j}(k-1)]\cdots \quad (18)$$

Equation(18) means that, if (i,j) always lies in the strong edge region, the probability of local same distribution will be very small.

If the value of (i,j) changes very little in time domain, it usually means that the IRFPA does not move. Then $\theta_{i,j}(k)$ calculated from these data will lead to a wrong result. Define[3, 11]

$$p_{mv}[Y_{i,j}(k-n+1:k)] = \begin{cases} 1 & \mathrm{std}[y_{i,j}(k-n+1:k)] > \sigma_{mv} \\ 0 & \mathrm{std}[y_{i,j}(k-n+1:k)] \leqslant \sigma_{mv} \end{cases}, \quad (19)$$

$p_{mv}[Y_{i,j}(k-n+1:k)]$ is the probability whether the IRFPA has moved. $\mathrm{std}(\bullet)$ is the operator to calculate (i,j) temporal standard deviation from frame $k-n+1$ to frame k. σ_{mv} is a threshold of the temporal standard deviation. σ_{mv} must be larger than the standard deviation of the dynamic noise σ_{noise}. Usually set $\sigma_{mv} = 3\sigma_{noise}$. $y_{i,j}(k-n+1:k)$ is (i,j)'s value from frame $k-n+1$ to frame k.

$$\mathrm{std}[y_{i,j}(k-n+1:k)] = \sqrt{\frac{\sum_{p=k-n+1}^{k}\left[y_{i,j}(p) - \left[\sum_{q=k-n+1}^{k} y_{i,j}(q)/n\right]\right]^2}{n}}. \quad (20)$$

And the final prior probability $p[\kappa_{i,j}(k)\,|\,Y_{i,j}^{k}]$ should be the combination of $p[\kappa_{i,j}(k-1)\,|\,\theta_{i,j}(k-1), Y_{i,j}^{k-1}]$, p_{lsd} and p_{mv}.

$$p[\kappa_{i,j}(k)\,|\,Y_{i,j}^{k}] = p[\kappa_{i,j}(k-1)\,|\,\theta_{i,j}(k-1), Y_{i,j}^{k-1}]\,p_{lsd}[Y_{i,j}(k)]\,p_{mv}[Y_{i,j}(k-n+1:k)]. \quad (21)$$

When the prior probability has been designed, the next task is to design the observation probability. In fact, we have already designed the observation probability. Equation (14) in Section 3 is the observation probabilityof the nonuniformity parameter.

$$p[\theta_{i,j}(k)\,\kappa_{i,j}(k), Y_{i,j}^{k}] = \frac{1}{\sqrt{2\pi}\,sd_{i,j}}\exp\left[-\frac{(d_{i,j}(k) - m_{i,j})^2}{sd_{i,j}^{\,2}}\right], \quad (22)$$

and

$$d_{i,j}(k) = \mathrm{std}\Pi_O[\mathrm{gain}_{i,j}(k)] = \sqrt{\frac{\sum_{p=i-o}^{i+o}\sum_{q=j-o}^{j+o}\left\{\mathrm{gain}_{p,q}(k) - \left[\sum_{g=i-o}^{i+o}\sum_{f=j-o}^{j+o}\mathrm{gain}_{g,f}(k)/(2o+1)^2\right]\right\}^2}{(2o+1)^2}}. \quad (23)$$

Equation (24) means that according to the space relativity of the IRFPA gain, the gain parameters in local region will change very small. If the gain changes evidently, the right probability should be very small.

$\theta_{i,j}(k)$ is calculated from frame $k-n+1$ to k. When the right probability $p[\kappa_{i,j}(k)\,|\,\theta_{i,j}(k), Y_{i,j}{}^{k}]$ is gotten, it can be used to update the final NUC parameters. $\psi_{i,j}(k)$ is defined as the NUC parameters which are finally used to correct the nonuniformitym. $\psi_{i,j}(k)$ should be updated by $\theta_{i,j}(k)$'s right probability.

$$\psi_{i,j}(k) = \psi_{i,j}(k-1)\{1 - p[\kappa_{i,j}(k)\,|\,\theta_{i,j}(k), Y_{i,j}{}^{k}]\} + \theta_{i,j}(k)\,p[\kappa_{i,j}(k)\,|\,\theta_{i,j}(k), Y_{i,j}{}^{k}]. \quad (24)$$

4 Experiments and results

In order to evaluate the processing effect, a real image sequences $S^1 = \{I_1^1, I_2^1, \cdots I_k^1, \cdots, I_{500}^1\}$ (acquired

at the rate 50 Hz by Sofradir MARS long-wavelength 320×256 HgCdTe IRFPA) was used to verify our algorithm. These images contain sky-scene and ground-scene.

We compared the Bayesian CS algorithm with the CS algorithm at the sky scene. Figure 4 is the comparison of two algorithms at the 20th frame. Twenty frames are enough for Bayesian CS algorithm to converge, while the CS algorithm can not converge with only 20 frames. In this IRFPA, σ_{noise} is 3. n is set to 20. When O is set larger than 5, its effect is the same as $O=5$. So we set $O=5$.

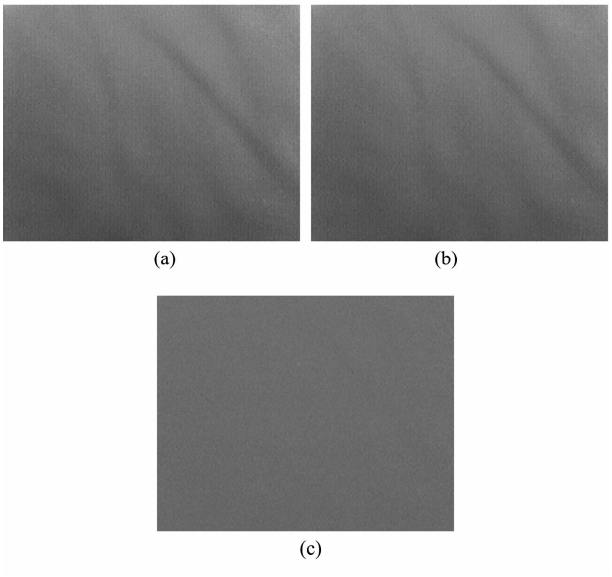

Fig. 4 Comparison of two algorithms at the 20th frame (sky-scene) (a) original image, (b) the CS algorithm, and (c) the Bayesian CS algorithm.
图4 两种算法处理效果比较(第20帧,天空背景)(a) 原始图像,(b) CS算法处理效果,(c) Bayesian CS算法处理效果

Figure 5 is comparison of two algorithms at the sky and ground scene. The CS algorithm has serious ghosting artifacts, while the Bayesian CS algorithm has almost no ghosting artifacts.

Figure 6 is the right probability of Bayesian CS algorithm of Fig. 5. The right probability in the sky is high, while the right probability in the ground is very small. This determines that the Bayesian CS algorithm's right probability is high at the sky-scene and low at the ground-scene. Usually, the nonuniformity is very serious in the sky, while it almost can not be seen in the ground. So, it can be seen that the Bayesian CS algorithm will be very effective in the real application.

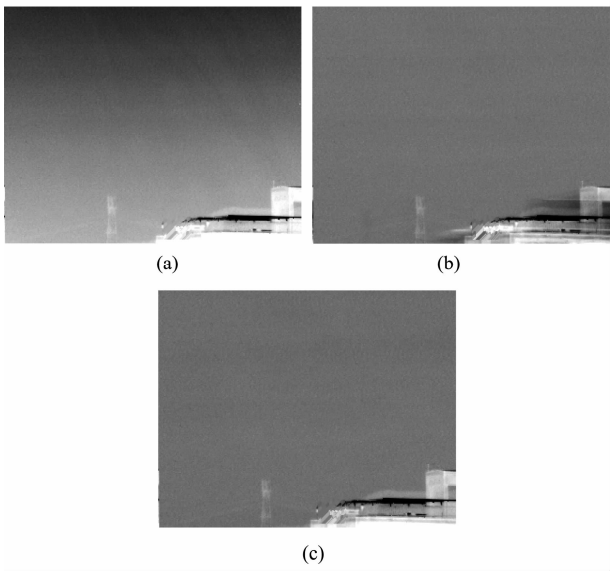

Fig. 5 Two algorithms' comparison at the sky and ground scene. (a) original image, (b) the CS algorithm, and (c) the Bayesian CS algorithm
图5 两种算法处理效果比较(天地交界背景)(a) 原始图像,(b) CS算法处理效果,(c) Bayesian CS算法处理效果

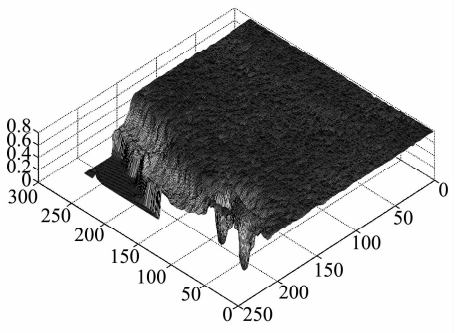

Fig. 6 The right probability of the Bayesian CS algorithm
图6 Bayesian CS算法的非均匀性参数正确概率

It is easy to calculate the NUC parameters in the sky-scene, and difficult in the ground-scene. So we will pay much more attention to the ground-scene. We use a real image sequence $S^2=\{I_1^2, I_2^2, \cdots I_k^2, \cdots, I_{490}^2\}$ to analyze our algorithm, and these are ground-scene images without nonuniformity. The virtual nonuniformity is added to these images. The nonuniformity gain obeys Gaussian distribution (mean is 1 and standard deviation is 0.005), offset obeys Gaussian distribution (mean is 0 and standard deviation is 6). Set $m_{i,j}=0.005$ and

$sd_{i,j}=0.005$. Figure 7 is the processing result.

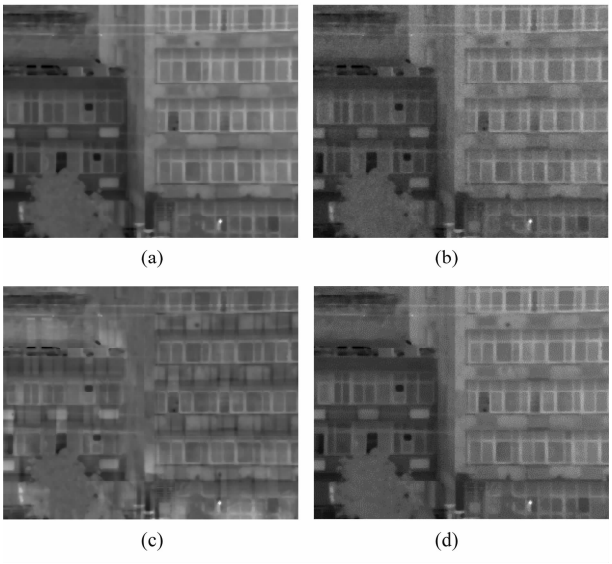

Fig. 7 Processing Result of real image with virtual nonuniformity (a) original image without nonuniformity, (b) original image added with nonuniformity, (c) the CS algorithm, and (d) the Bayesian CS algorithm
图 7 真实图像叠加虚拟非均匀性噪声的处理效果 (a) 原始图像不包含非均匀性噪声, (b) 原始图像叠加非均匀性噪声, (c) CS 算法处理效果, (d) Bayesian CS 算法处理效果

From Fig. 7, it can be seen that the CS algorithm has serious ghosting artifacts in the complex ground-scene. While the Bayesian CS algorithm can effectively eliminate the nonunformity and has no ghosting artifacts. We use MSE to compare the processed result[10].

Figure 8 shows variations two algorithms' MSE with time.

It can be seen that after 250 frames, the Bayesian CS algorithm begin to converge, while the CS algorithm can not. The Bayesian CS algorithm uses tens of frames to converge in the sky-scene, and hundreds of frames in the ground-scene. This adaptive control comes from the Bayesian right probability.

5 Conclusions

The connection between the scene-based parameters and the reference-based parameters has been presented in this paper, which is the Bayesian right probability. The convergence speed and ghosting artifacts of the estimates obtained were derived and verified by

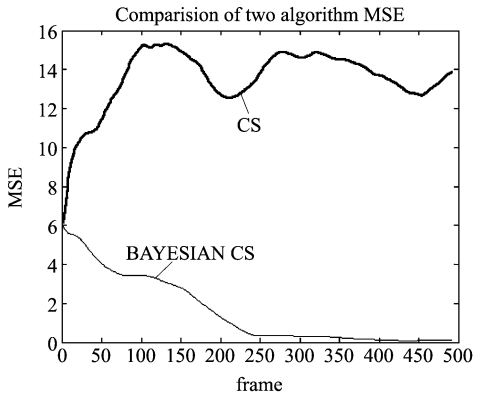

Fig. 8 The MSE chang of the two algorithms' with frames
图 8 两种算法的 MSE 随时间变化曲线

simulations. The calibration results of our algorithm were also demonstrated using real and simulated infrared image sequences, and the experiments verified our algorithm's good effect.

The nonuniformity space relativity characteristic of gain summarized by this paper is a very important characteristic, and makes more contribution to the nonuniformity correction.

The right probability can determine whether the calculated scene-based NUC parameters are correct or not. According to the mechanism of the Bayesian right probability, we can construct the right probability for other NUC algorithms, such as the LMS NUC algorithm and etc. And last but not least, the Bayesian right probability can be constructed as a connection to link different scene-based NUC algorithms. The combination of different NUC algorithms can help each other and get better processing effect together.

REFERENCES

[1] Scribner D A, Sarkady K A, Caulfield J T. Adaptive retina-like preprocessing for imaging detector arrays [J]. *Proc. IEEE Int. Conf. Neural Networks*, San Francisco, USA, 1993: 1955 - 1960.

[2] Scribner D A, Sarkady K A, Caulfield J T. Nonuniformity correction for staring IR focal plane arrays using scene-based techniques [J]. *Proc. SPIE*, 1990, **1308**: 224 - 233.

[3] Harris J G, Chiang Y M. Nonuniformity correction of infrared image sequences using the constant-statistics constraint [J]. *IEEE Transactions on Image Processing*, 1999, **8** (8): 1148 - 1151.

[4] Zhang C, Zhao W - Y. Scene - based nonuniformity correction

(下转第 507 页)

射能量,但天空背景大气的辐射能量较弱,可以忽略. 土壤自身热辐射的偏振特性很弱,含水土壤表面的偏振特性主要是太阳光的反射作用所引起,其中,2 400 ~3 000 cm^{-1}波段内太阳光的能量较强,在一定太阳光照射和仪器观测条件下,土壤表面的偏振度随含水量增加而增大,可以建立土壤含水量与偏振度之间的相关关系,为土壤含水量的遥感反演提供一种新方法.

REFERENCES

[1] Curran P J. A photographic method for the recording of polarised visible light for soil surface moisture indications[J]. *Remote Sensing of Enviroment*, 1978,**7**(4): 305 - 322.

[2] Curran P J. The use of polarized panchromatic and false-color infrared film on the monitoring of soil surface moisture [J]. *Remote Sensing of Enviroment*, 1979, **8**(3): 249 - 266.

[3] Curran P J. Remote sensing: the use of polarized visible light (PVL) to estimate surface soil[J]. *Applied Geography*, 1981, 1: 41 - 53.

[4] Genda H, Okayama H. Simulator for remote sensing and its application to soil moisture measurements[J]. *Applied Optics*, 1978, **17**(5): 807 - 813.

[5] Genda H, Okayama H. Estimation of soil moisture and components by measuring the degree of spectral polarization with a remote sensing simulator[J]. *Applied Optics*, 1978, **17**(21): 3439 - 3443.

[6] Breon F M, Tanre D, Lecomte P, *et al*. Polarized reflectance of bare soils and vegetation: Measurements and Models[J]. *IEEE Transactions on Geoscience and Remote Sensing*, 1995, **33**(2): 487 - 499.

[7] SONG Kai-Shan, ZHAO Yun-Shen, ZHANG Bo. The polarized reflectance characteristics of some soils[J]. *Chinese Journal of Soil Science*(宋开山, 赵云升, 张柏. 土壤偏振反射特性的多角度测量与研究. **土壤通报**), 2004, **35**(4): 420 - 425.

[8] Zhang Q, Sun X B, Li Y N, *et al*. Quasi-quantitative relationship between soil moisture and polarization characteristics[J]. *Journal of Remote Sensing*, 2010, **14**(6): 1067 - 1073.

[9] Sandus O. A review of emission polarization[J]. *Applied Optics*, 1965, **4**(12): 1643 - 1652.

[10] Shaw J A. Degree of linear polarization in spectral radiances from water-viewing infrared radiometers[J]. *Applied Optics*, 1999, **38**(15): 3157 - 3166.

[11] Shaw J A. Infrared polarization in the natural earth environment[J]. *Proc. Of SPIE*, 2002, **4819**: 129 - 138.

[12] Cooper A W, Lentz W J, Walker P L. Infrared polarization ship images and contrast in the maptip experiment [J]. *Proc. Of SPIE*, 1996, **2828**: 85 - 96.

[13] WANG Zhen, QIAO Yan-Li, HONG Jin, *et al*. Detecting camouflaged objects with thermal polarization imaging system[J]. *Infrared and Laser Engineering*(汪震, 乔延利, 洪津,等. 利用热红外偏振成像技术识别伪装目标. **红外与激光工程**), 2007, **36**(6): 853 - 856.

[14] YUAN Yue-Ming, XIONG Wei, FANG Yong-Hua, *et al*. Detection of oil spills on water by differential polarization FTIR spectrometry[J]. *Spectroscopy and Spectral Analysis*(袁越明, 熊伟, 方勇华,等. 差分偏振 FTIR 光谱法探测水面溢油污染. **光谱学与光谱分析**), 2010. **30**(08): 2129 - 2132.

[15] ZHANG Jian-Qi, FANG Xiao-Ping. *Infrared physics*[M]. Xi'an: Xidian University Publishing House(张建奇, 方小平. **红外物理**). 西安: 西安电子科技大学出版社, 2004:71.

[16] SHAO Ming-An, WANG Quan-Jiu, HUANG Ming-Bin. *Soil physics*[M]. Beijing: Higher Education press(邵明安, 王全九, 黄明斌. **土壤物理学**),. 北京: 高等教育出版社,2006: 56.

[17] Torrance K E, Sparrow E M. Theory for off-specular reflection from roughened surfaces[J]. *Journal of the optical society of America*, 1967, **57**(9): 1105 - 1114.

(上接497 页)

using local constant statistics[J]. *J. Opt. Soc. Am. A*, 2008, **25**(6): 1444 - 1453.

[5] Torres S N , Hayat M M. Kalman filtering for adaptive nonuniformity correction in infrared focal-plane arrays [J]. *Opt. Soc. Am. A*, 2003, **20**(3): 470 - 480.

[6] Shehadeh M , Kuybeda O. Robust nonuniformity correction in infrared images[J]. *Proc. IEEE Int. Conf. Electrical and Electronics Engineers, Israel*, 2008: 275 - 279.

[7] Qian W X, Chen Q, Gu G-H. Space low-pass and temporal high-pass nonuniformity correction Algorithm[J]. *Optical Review*, 2010, **17**(11): 24 - 29.

[8] Qian W X, Chen Q, Gu G-H, *et al*. Correction method for stripe nonuniformity[J]. *Applied Optics*, 2010, **49**(10): 1764 - 1773.

[9] Parker D R, Gustafson S C, Oxley M E, *et al*. Development of a Bayesian framework for determining uncertainty in receiver operating characteristic curve estimates [J]. *IEEE Transactions on Knowledge and Data Engineering*, 2010, **22**(1): 31 - 45.

[10] Celik T. Change detection in satellite images using a genetic algorithm approach[J]. *IEEE Geoscience and Remote Sensing Letters*, 2010, **17**(2): 386 - 390.

[11] Hardie R C , Baxley F , Brys B, *et al*. Scene-based nonuniformity correction with reduced ghosting using a gated LMS algorithm [J]. *Optical Express*, 2009, **17** (17): 14918 - 14933.

[12] Torres S N , Hayat M M. Kalman filtering for adaptive nonuniformity correction in infrared focal plane arrays[J]. *The Journal of the Optical Society of America A* 2003, **20**(3): 470 - 480.

[13] Torres S N , Vera E M, Reeves R A, *et al*. Adaptive scene-based nonuniformity correction method for infrared focal plane arrays[J]. *SPIE Conference on Infrared Imaging Systems: Design Analysis*, Modeling, and Testing XIV, Orlando, Florida, 2003, **5076**: 75 - 80.

[14] Vera E M, Torres S N. Fast adaptive nonuniformity correction for infrared focal-plane array detectors[J]. *Eurasip Journal on Applied Signal Processing* 2005, **13**: 1994 - 2004.